Journal of Science: Advanced Materials and Devices 11 (2026) 101085

Contents lists available at ScienceDirect

Journal of Science: Advanced Materials and Devices

journal homepage: www.elsevier.com/locate/jsamd

Research Article

Glycine-functionalized $Ti_3C_2T_x$ MXene with improved material properties for concurrent Sn^{2+} oxidation mitigation and defect passivation in efficient tin halide perovskite solar cells

Aseel j. Mohammed [a], Wala Dizayee [b], Ismail Ibrahim Marhoon [c], Mohammed Ahmed Mohammed [d], Mohammed Zorah [e], Zainab Shaker Matar Al-Husseini [f], Mohamed Shabbir Abdulnabi [g,*], G. Abdulkareem-Alsultan [h,**], Maadh Fawzi Nassar [h,***]

[a] College of Electromechanical Engineering, University of Technology-Iraq, Baghdad, Iraq
[b] Department of General Sciences, College of Basic Education, Salahaddin University-Erbil, Erbil, Kurdistan Region, Iraq
[c] Materials Engineering Department, College of Engineering, Mustansiriyah University, Baghdad, Iraq
[d] Department of Medical Physics, College of Science, University of Al-Qadisiyah, Al-Qadisiyah, Iraq
[e] Department of C. T. E, Imam Alkadhim University College, Baghdad, Iraq
[f] Laboratory of Signals, Systems, Artificial Intelligence and Networks (SM@RTS), Digital Research Center of Sfax, University of Sfax, Sfax, Tunisia
[g] School of Technology, Asia Pacific University of Technology and Innovation (APU), 57000, Kuala Lumpur, Malaysia
[h] Department of Chemistry, Faculty of Science, Universiti Putra Malaysia, UPM, Serdang, 43400, Selangor, Malaysia

ARTICLE INFO

Keywords:
$Ti_3C_2T_x$
MXene
Defect passivation
Perovskite solar cells
PSCs

ABSTRACT

Lead-free tin halide perovskites constitute a nontoxic alternative to lead-based solar absorbers, but their development is stifled by low performance and material instability, attributed primarily to Sn^{2+} oxidation, high levels of defects, and slow charge transfer. We demonstrate glycine-functionalized $Ti_3C_2T_x$ MXene (MXG) as a multifunctional additive in $FASnI_3$ perovskite films. The amino groups on MXG have a two-fold role in that they chemically passivate the under-coordinated Sn sites and iodine vacancies, while at the same time providing moderate reductants to suppress Sn^{2+} oxidation. Aside from passivation, the MXene with layered conductive properties also acts as a favorable template for perovskite crystallization, allowing the vertical grain orientation for better light absorption into the absorber layer, improveing interfacial connection between layers and charge carrier transfer/extraction. For the MXG devices, better film quality and reduced trap state density and carrier lifetime with enhanced energy level alignment were observed. The champion MXG/$FASnI_3$ device shows a power conversion efficiency of 15.82 % with improved stability (maintaining over 94 % of its initial efficiency after 1000 h). This investigation highlights the dual electrical and structural benefits of MXene engineering toward achieving earth-abundant, efficient, stable, and scalable Sn perovskite PVs.

1. Introduction

Sn-free Halide perovskites are gaining interest as green photovoltaic absorbents, but their device efficiency is still lagging in comparison to efficiency levels of lead perovskites due to issues associated with oxidized Sn(II)& structural instability [1,2]. Hydrazine which is a classic hazardous reducing agent has now found an application in the making of Sn-based ABO3 perovskite films as the first efficient reduction reagent for this purpose because it is not only used but also consumed by Sn4+ in stoichiometric compositions to produce only tin2 thereby disallowing the formation of Sn4+ which is not acceptable if it exists without surplus of other element making up AB(O)3 but hydrazine also had to deal with practical issues [3]. Recent studies have investigated benign additives and passivation techniques to enhance film quality and durability [4]. Qiu et al. have demonstrated one of the multifunctional organic molecules (MATC) as a perovskite additive, which reduced defect states and

* Corresponding author.
** Corresponding author.
*** Corresponding author.
E-mail addresses: mohamed.shabbir@apu.edu.my (M.S. Abdulnabi), kreem.alsultan@yahoo.com (G. Abdulkareem-Alsultan), nassarmaadh@gmail.com (M.F. Nassar).

https://doi.org/10.1016/j.jsamd.2025.101085
Received 28 September 2025; Received in revised form 16 December 2025; Accepted 17 December 2025
Available online 19 December 2025

increased the power conversion efficiency up to around 21.5 % with significantly improved device stability [5]. In a similar vein, Xia et al. reported that the use of tailor-made hydrazine derivatives in printable HCF carbon solar cells achieved high efficiencies and efficient defect passivation in a saleable low cost mesoscopic architecture [6]. These techniques suppress trap-assisted recombination, but without the hazards associated with neat hydrazine.

In order to mitigate tin oxidation and ion migration, concurrent attempts concentrate on structural and interfacial modifications [7]. The immobilization of ions and the inhibition of Sn-induced defects have been demonstrated through the incorporation of reduced-dimensional (2D) perovskite phases or spacers [8]. In a mixed Sn–Pb perovskite, Liu et al. [3] reported a synergistic strategy that combined bulk hydrazinium chloride (N_2H_5Cl) doping with ethylene diammonium diiodide (EDADI) surface treatment. This strategy anchored iodide ions and suppressed Sn(II) oxidation. The result was a low-bandgap cell with a champion 23.2 % PCE (which was used in tandem to achieve a total of 28.3 %) and negligible hysteresis, indicating a significantly reduced rate of ionic migration. Zeng et al. enhanced the device's power conversion efficiency (PCE) by approximately 48 % and extended its operational longevity by doping it with 2,4-dichlorophenylhydrazine hydrochloride, resulting in a "self-repairing" $FASnI_3$ perovskite [9]. Zhang et al. achieved a significant increase in air stability in a separate study by incorporating chloride to induce an in situ 2D layered perovskite capping phase [10]. This phase acts as an n-type moisture barrier, stopping the Sn–perovskite film from breaking down [10]. Moreover, the performance of tin-perovskite cells can be enhanced by improving the charge-transport layers. Mu et al. showed that adding a porphyrin supramolecule to the hole-transport layer enhanced its conductivity by a factor of ten. This made the layer more efficient (going from about 20 % to 23.2 %) and more stable at high temperatures [11].

Although these achievements are remarkable, most of the procedures rely heavily on the use of molecular dopants or external doping approaches, which often meet problems relating to compatibility with the benchmark processability and long-term chemical stability issues with the perovskite host. Moreover, despite the performance enhancements, the practical translation of many of them is still limited by complicated post-treatments or toxic analogues of hydrazine [12–16].

In this context, materials with two dimensions (2D), mainly MXenes, have emerged as important multifunctional platforms in the production of perovskite solar cells. MXene $Ti_3C_2T_x$ gives the best combination of increased electronic conductivity, surface modifiability, and the ability to coexist with perovskite surfaces. [17–20]. Its multi-layered architecture and hydrophilic surface allow it to distribute smoothly within the perovskite matrix or align itself where interface control is most needed. [21,22]. Recent findings demonstrate the utilization of pure or modified MXenes in lead-based perovskite solar cells to enhance charge extraction, reduce non-radiative recombination, and improve environmental stability [23–25]. However, their applications in lead-free Sn-based perovskite systems have rarely been explored, especially for chemical passivation and oxidation protection purposes. The amino-functionalization of $Ti_3C_2T_x$ MXene is interesting, given that terminal $–NH_2$ groups have a dual role (1) acting as mild reducing agents to regulate Sn^{2+} oxidation; and (2) as Lewis bases used for the coordination with under-coordinated Sn atoms and iodine vacancies, thereby passivating defects. This approach provides a non-toxic, thermally stable and structurally suitable alternative to the molecular hydrogen containing additives such as hydrazine derivatives or thiols [7]. Similarly, the conjugated interface made by amino-functionalized MXene can improve energy level alignment, speed up perovskite crystallization, and slow down ion migration. All of these things are important for fixing difficulties that are common in tin-based perovskite photovoltaics.

Herein, we describe the rational design and incorporation of amino-functionalized $Ti_3C_2T_x$ MXene nanosheets in $FASnI_3$ perovskite films. We investigate the chemical interaction of MXene with Sn-based perovskite precursors, the effect of functionalization on film quality, and device performance and stability in ambient and under thermal stress. We found that employing amino functionalized MXene can significantly improve the device efficiency and shelf-stability due to simultaneous fault-passivation and Sn^{2+} oxidation retardation. This research highlights a new road in multitask material design for lead-free perovskite solar cells and introduces a green, scalable approach toward high-performance tin-based photovoltaic technology.

2. Experimental

2.1. Preparation of glycine-functionalized $Ti_3C_2T_x$ MXene ($Ti_3C_2T_x$–NH_2)

We got titanium aluminum carbide (Ti_3AlC_2, >98 %, 400 mesh), lithium fluoride (LiF, 98 %), hydrochloric acid (HCl, 37 %), glycine (≥99 %), ethanol (EtOH), and deionized water (18.2 MΩ cm) from Sigma-Aldrich and used them without any extra purification.

2.1.1. Synthesis of $Ti_3C_2T_x$ MXene

The synthesis of $Ti_3C_2T_x$ MXene was accomplished by the selective etching of aluminum from the Ti_3AlC_2 MAX phase using a minimally invasive layer delamination (MILD) technique. The etching solution was prepared by gradually adding 1g of LiF to 20 mL of 9M HCl at room temperature and simultaneously stirring. After that, 1 g of Ti_3AlC_2 powder was added to the solution in 10 min, and the mixture was kept at 35 °C for 24 h. The resultant suspension was periodically rinsed with deionized water and subjected to centrifugation (3500 rpm, 10 min) until the supernatant approached a near-neutral pH (~6). The precipitate was subsequently redispersed in deionized water and sonicated for 1 h in an argon environment to delaminate the $Ti_3C_2T_x$ sheets. The culture was centrifuged at 3500 rpm for 30 min to exclude unexfoliated particles, and the dark supernatant containing single- or few-layer $Ti_3C_2T_x$ nanosheets was obtained.

2.1.2. Amino-functionalization with glycine

To synthesize glycine-functionalized MXene, 20 mL of the $Ti_3C_2T_x$ colloidal suspension (5 mg mL^{-1}) was combined with 50 mg of glycine while maintaining continuous agitation. The mixture was agitated at ambient temperature for 12 h to facilitate covalent interaction between the amino groups of glycine and the surface-terminated groups (–OH, –F) on $Ti_3C_2T_x$ by condensation or hydrogen bonding [26]. The resultant product, $Ti_3C_2T_x$–NH_2, was obtained via centrifugation (10,000 rpm, 15 min), subsequently washed with ethanol and DI water to eliminate surplus glycine, and dried under vacuum at 60 °C for 12 h.

2.2. Fabrication of tin-based perovskite solar cells

Inverted (p–i–n) planar heterojunction devices were fabricated with the structure:

ITO/PEDOT:PSS/$FASnI_3$ + $Ti_3C_2T_x$–NH_2/PCBM/BCP/Ag.

2.2.1. Substrate preparation

Indium tin oxide (ITO)-coated glass substrates were sequentially cleaned by ultrasonication in detergent, deionized water, acetone, and isopropanol for 15 min each. Post-cleaning, the substrates underwent UV–ozone treatment for 15 min to enhance surface wettability.

2.2.2. Hole transport layer (HTL) deposition

A filtered aqueous solution of PEDOT:PSS was spin-coated onto the cleaned ITO substrates at 4000 rpm for 30 s. The coated substrates were subsequently annealed at 150 °C for 15 min in ambient air to create a consistent HTL.

2.2.3. Perovskite layer formation

The perovskite precursor solution was prepared by dissolving formamidinium iodide (FAI) and tin(II) iodide (SnI_2) in a mixed solvent of dimethylformamide (DMF):dimethyl sulfoxide (DMSO) at a volume ratio of 4:1. To suppress the Sn^{2+} oxidation and improve film quality, 10 mol% SnF_2 and 1 mol% excess FAI were added to the solution. The precursor solution was stirred in nitrogen for several hours to ensure the solid was completely dissolved. The perovskite layer was prepared by two-step spincoating: 1000 rpm for 10 s first, and then 4000 rpm for another 30 s. In the last 10 s of the second step, 200 μL chlorobenzene was dropped onto the spinning substrate while it was rotating to act as an antisolvent to promote rapid crystallization. The films(whose resulting MAPbI3 perovskite was grown by the film initial annealing at 100 °C for 10 min in a nitrogen-filled glovebox) were then finally annealed at 100 °C for 10 min to complete growth of the perovskite layer.

2.2.4. Electron transport layer (ETL) deposition

A solution of phenyl-C_{61}-butyric acid methyl ester (PCBM) in chlorobenzene (20 mg mL^{-1}) was spin-coated onto the perovskite layer at 2000 rpm for 30 s to serve as the electron transport layer (ETL). A 0.5 mg mL^{-1} solution of bathocuproine (BCP) in isopropanol was then spin-coated at 5000 rpm for 30 s to act as a buffer layer between the metal electrode and the electron transport layer (ETL). To integrate MXG into the perovskite absorber, a glycine-functionalized MXene stock solution was initially produced by dispersing MXG in a DMF/DMSO (4:1 v/v) solvent combination at a concentration of 1.0 mg mL^{-1}, followed by sonication for 1 h. Aliquots of this stock were subsequently added to the $FASnI_3$ precursor to achieve final MXG concentrations of 0.05, 0.10, 0.15, 0.20, and 0.25 mg mL^{-1}. The films and devices produced from these concentrations were assessed using SEM/AFM morphological mapping, XRD/GIWAXS crystallinity analysis, SCLC-derived trap density measurements, and comprehensive photovoltaic characterization. An MXG loading of 0.10 mg mL^{-1} was determined to produce the best combination of increased grain size, diminished microstrain, minimized trap density, and superior device performance (PCE and Voc). This optimum concentration was employed for all MXG/$FASnI_3$ devices documented in this investigation.

2.2.5. Top electrode deposition

A shadow mask was used to thermally evaporate a 100 nm thick coating of silver (Ag) onto the device in a high vacuum environment (about 1×10^{-6} Torr). This created an active area of 0.1 cm^2.

2.2.6. Encapsulation

To prevent environmental degradation, the devices were encapsulated with a UV-curable epoxy and sealed with a cover glass before being taken out of the glovebox for characterization.

2.3. Characterization

The crystallinity of the as-prepared Mxene and perovskite films was investigated using Bruker X-ray diffraction (XRD) with a Cu Kα radiation light source (λ = 1.5406 Å). Surface and cross-sectional morphologies were observed with a Hitachi SU70 field-emission scanning electron microscope (FE-SEM). Surface roughness and topography were characterized with atomic force microscopy (AFM). The optical bandgap and absorption nature were recorded using the Thermo Fisher Scientific spectrophotometer from UV–Vis (200–800 nm) absorbance spectra. Nexsa X-ray photoelectron spectroscopy (XPS) was carried out to analyze the elemental composition and chemical states of the perovskite films. FTIR spectroscopy was used to identify functional groups and confirm chemical bonding in the materials. During luminescence testing, steady-state photoluminescence (PL) measurements were carried out on the Hitachi F-7000 spectrometer to determine the emission properties and defect states. Carrier lifetimes and recombination dynamics were studied by time-resolved photoluminescence (TRPL) spectroscopy. The current–voltage (J–V) characteristics of as-prepared solar cells were measured using a (Model M101, Autolab) under the solar simulator (Instytut Fotonowy, Poland) were measured at simulated AM 1.5G sunshine with an intensity of 100 mW/cm^2. The wavelength-dependent photoresponse was measured by the external quantum efficiency (EQE) spectra. Charge transport and recombination mechanisms in the devices were studied using electrochemical impedance spectroscopy (EIS).

3. Result and discussion

To gain insight into the fundamental role of MXG in influencing the characteristics of $FASnI_3$ perovskite films, we originally performed comprehensive structural and chemical analyses. The XRD patterns (Fig. 1a) show that the (002) reflection moves from 9.3° (MAX) to 5.8° (MXene) and then to 5.2° in MXG. [27,28]. This gradual downshift is in good agreement with the increase of interlayer distance from 9.49 Å to 15.22 Å, and to 17.00 Å, corresponding to the molecule intercalation as

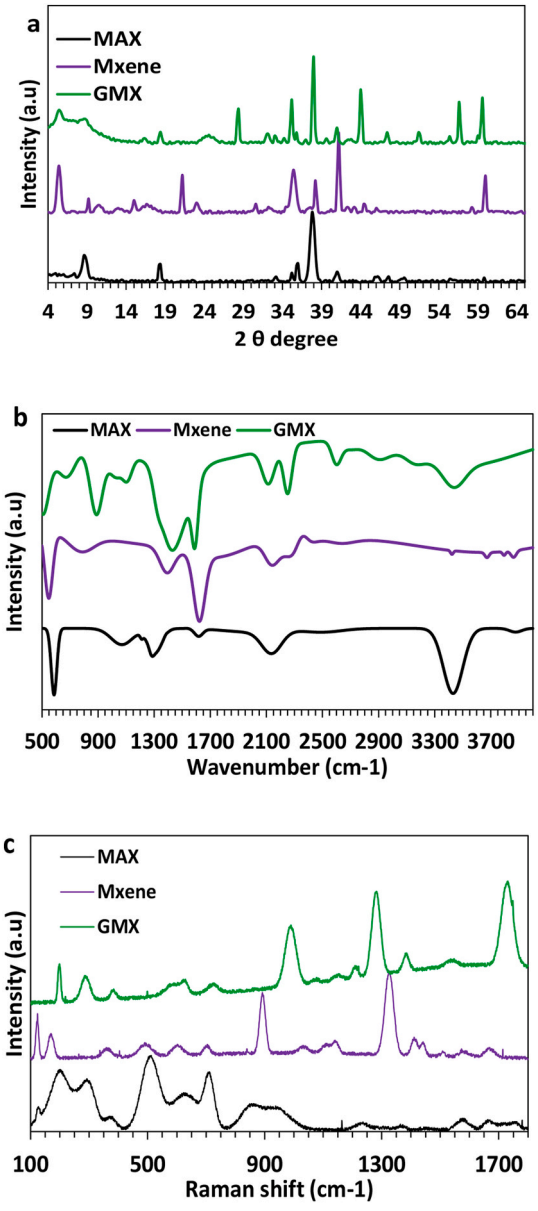

Fig. 1. (a) XRD patterns, (b) FTIR spectra, and (c)Raman spectra of MAX, MXene and MXG.

well as covalent grafting instead of pure physical adsorption. The increase of GF's d-spacing indicates the good insertion of glycine into the $Ti_3C_2T_x$ layers, and is consistent with previous studies on glycine-or amino acid-modified MXenes [28–30]. The FTIR analysis (Fig. 1b) has provided stronger evidence for the chemical bonding of glycine through the appearance of new bands at about 1640 cm^{-1} (N–H bending), 1400 cm^{-1} (C–N stretching), and 1030 cm^{-1} (Ti–O), besides a more pronounced O–H vibration at around 3430 cm^{-1}. Such features point to the formation of Ti–O–C covalent bonds resulting from the interaction of MXene –OH terminations and the –COOH group of glycine, as well as Ti–N coordination from the covalent bond of the $–NH_2$ group to the under-coordinated Ti sites through lone-pair donation. [31–33]. The complementary Raman spectra (Fig. 1c), retain the characteristic MXene peaks (200, 285, 368, 624 cm^{-1}) and develop new ones at 1148–1298 and 1445-1536 cm^{-1} from glycine inclusion, thus further confirming strengthened chemical bonding. The FTIR, Raman and XRD data together shows that glycine is attached to $Ti_3C_2T_x$ through a hybrid multimode binding: (i) covalent linkage of the zwitterionic amino acid with MXene; and (ii) development of supplementary hydrogen bonds between the glycine zwitterions backbone and the $Ti_3C_2T_x$ basal plane oxygens as well as surface terminations. [34,35]. This chemically integrated structure helps MXene spread out, makes surface dipole interactions stronger, and provides chemically active regions that help controlled perovskite nucleation and defect passivation [32,36].

Fig. 2a and b shows the phase transition of bulk MAX to multilayer MXene by SEM images. In the MAX phase (Fig. 2a), the layers are closely packed and no clear separation is observed, indexing to the Ti_3AlC_2 ~ Theoretical energy minimum (c/ã 4/3) ~ C-Al-A-Ti c a b Fig. After the HF etching and exfoliation procedure, the MXene (Fig. 2b), which has a larger interlayer distance and rolled up morphology, demonstrating well removal of the Al layers and exfoliation from $Ti_3C_2T_x$ sheets. The delamination step is important in providing a high surface-area/volume ratio that provides active edge and basal sites for further chemical functionalization [37–39]. The accordion-like shape and free space in MXene are important for glycine intercalation and surface functionalization to work well. [7,40]. The TEM image of MXG (Fig. 2c) shows he transformation of ultra-thin 2D nanosheets having visible flake edges. These flakes exhibit semi-transparency when subjected to electron beam exposure, signifying their few-layered composition [41]. The flakes show some transparency during electron beam treatment, which indicates that they are made of just a few layers. In addition, Fig. 2e presents convincing proof of glycine anchoring using high-resolution elemental mapping [30,33,42]. The regular coupling of N and C with Ti and Cr definitely indicates the effective grafting [43]. The nitrogen peak is especially important here, since it doesn't come from the MXene; instead, it reflects the $–NH_2$ groups contributed by glycine. [44,45]. This shows that glycine has made covalent or coordinative bonds with the MXene surface, perhaps through Ti–N or Ti–O–C connections [46–48].

In situ XRD was used to reveal the nucleation and crystal growth kinetics of $FASnI_3$ and MXG/$FASnI_3$ THP wet films during crystallization induced by post-annealing treatment in 2D/3D perovskite systems (Fig. 3a). The XRD patterns show the prominence of sharper and stronger peaks for MXG/$FASnI_3$ sample, especially at (100), (120), (200) and (300) planes, confirming higher crystalline nature coupled with larger grain size. The lower FWHM is indicative of better long-range order and phase purity. Unlike pure $FASnI_3$ where wide and less distinct peaks are observed, the introduction of MXG seems to promote a templated nucleation possibly due to the 2D lamellar structure acting as a template for crystal growth. The vertical orientation can be promoted by intercalated glycine and polar terminal groups and grain packing due to perovskite nucleation rate increasing, which is consistent with the observations registered in interface-directed crystallization of 2D/3D perovskite systems.

The detailed X-ray photoelectron spectroscopy (XPS) analysis was

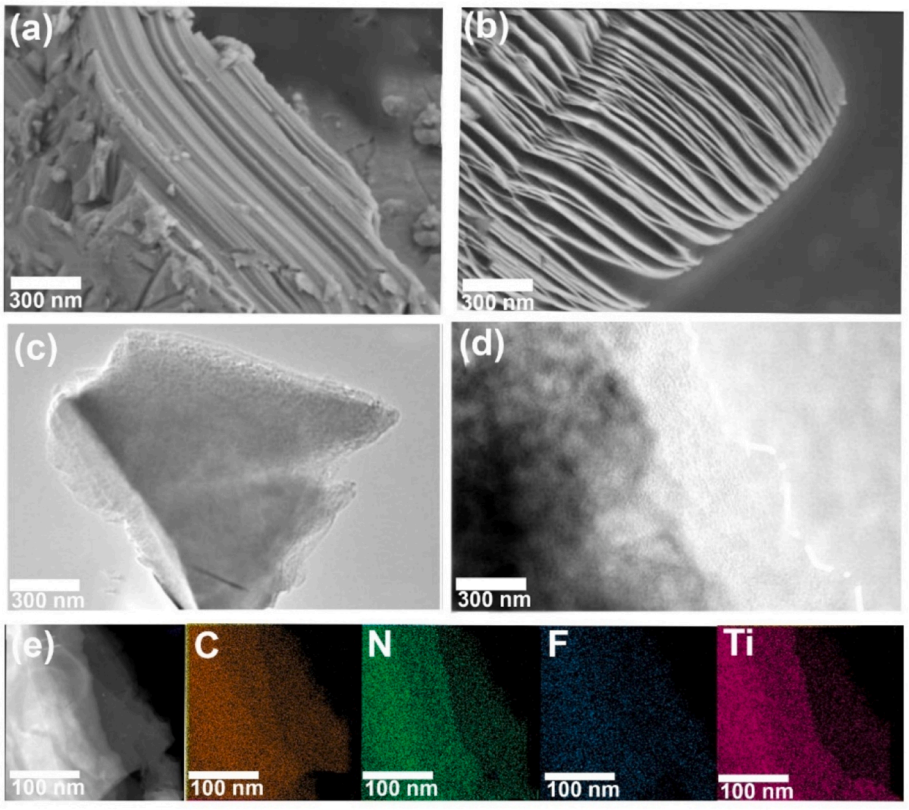

Fig. 2. (a) SEM image of multilayered MAX phase, and (b) MXene nanosheets; (c) TEM and (d) HRTEM images of MXG; (e) Elemental mapping of a selected MXG region showing uniform spatial distribution of C, N, F, and Ti in MXG.

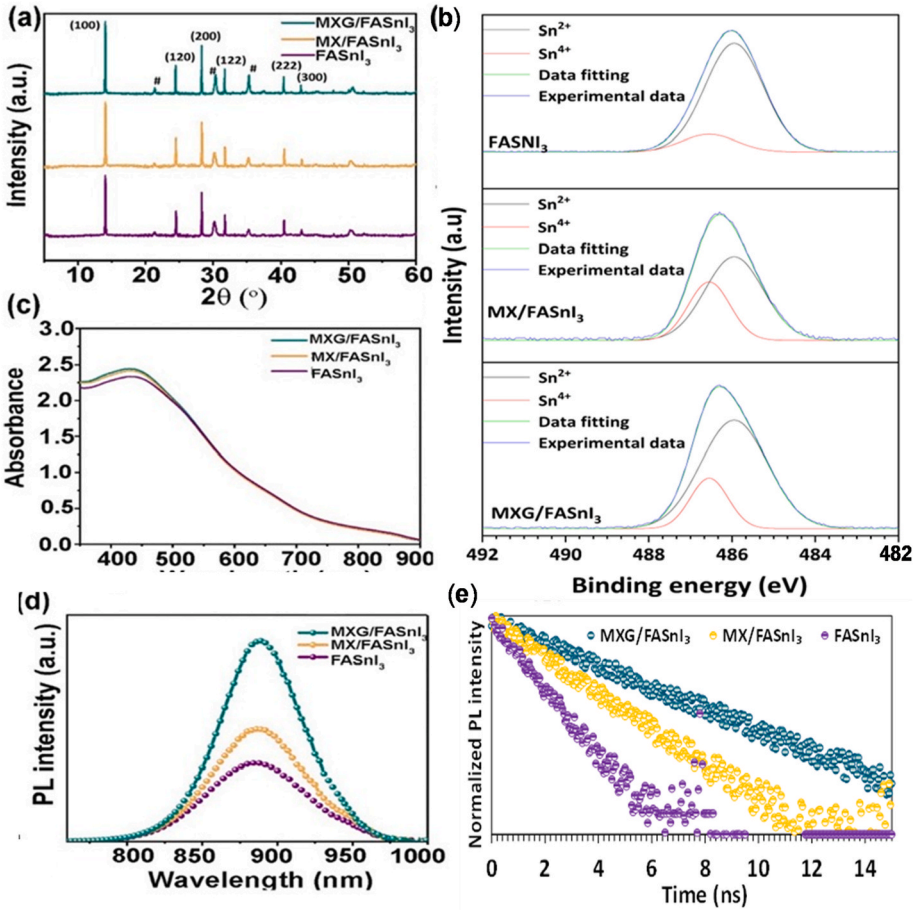

Fig. 3. Structural, optical, and charge carrier dynamics of three $FASnI_3$-based perovskite films (a) XRD patterns, (b) XPS spectra of Sn 3d core levels (c) UV–Vis absorbance spectra, (d) PL, and (e) TRPL spectra (f) KPFM-determined contact potential values of $FASnI_3$, $MX/FASnI_3$, and $MXG/FASnI_3$.

used to map the Sn4+ state distribution at the film surface and inside the bulk (Fig. 3b). The Sn 3d XPS peaks clearly separate the Sn^{2+} and Sn^{4+} species. The $FASnI_3$ sample shows a strong peak corresponding to Sn^{4+} whereas the $MX/FASnI_3$ shows a slight reduction in that and the $MXG/FASnI_3$ has the lowest amount of Sn^{4+}. The Sn^{4+}/Sn^{2+} ratio in MXG-treated films is notably lower confirming the antioxidant action of glycine-modified MXene. The electron-rich amine part of glycine forms a bond with the surface Sn atoms thereby giving rise to a shell-like protective coating that hinders the Sn atom's corroding power. The titanium atoms in MXene may also help in maintaining the oxidative atmosphere by acting like electrons in the circuit.

We performed ultraviolet–visible absorption (UV–vis), steady-state photoluminescence (PL), and time-resolved PL spectroscopy (TRPL) studies to examine the impact of the additives on the optical properties and to elucidate their function in the perovskite film. Because TRPL lifetimes are jointly governed by bulk defects, interfacial recombination, and charge-extraction kinetics, improvements in lifetime must be interpreted together with changes in band alignment and interfacial transport. Fig. 3c illustrates the UV–visible absorption spectra. All samples demonstrate comparable absorption onsets (~900 nm), indicating that the addition of neither MX nor MXG affects the bandgap of $FASnI_3$. The marginal enhancement in absorption magnitude in $MXG/FASnI_3$ indicates improved light-harvesting efficiency attributed to diminished surface defects and scattering. Additionally, we conducted PL and TRPL studies to investigate the charge dynamics in the presence of MX nor MXG. Fig. 3c illustrates the PL spectrum. No substantial alteration in the bandgap was observed; nevertheless, the treated perovskite films demonstrated a marked increase in photoluminescence intensity relative to the control film, suggesting a decrease in effective non-radiative trap-assisted recombination. Considering that the absorption coefficient in Sn-based perovskites may reach approximately $3.9 \times 10^4\ cm^{-1}$, and the film thickness is roughly 200 nm, carriers are evenly photogenerated across the entire film thickness. Consequently, trap states situated at the grain boundaries may serve as the primary non-radiative pathways, surpassing those found at the perovskite surface. The TRPL spectra (refer to Fig. 3d) were fitted using a biexponential decay function represented by the subsequent formula [49]:

$$I(t) = A_1 e^{-t/\tau_1} + A_2 e^{-t/\tau_2} \quad (1)$$

τ_1 represents the rapid decay component, while τ_2 denotes the gradual decay component, as found in other non-lead compounds. The optimal fitting parameters are presented in Table S1. The τ_1 range was extended from 0.4 ns ($FAMASnI_3$) to 1.45 ns ($MX/FAMASnI_3$) and 2.12 ns ($MXG/FAMASnI_3$). Considering the significant heterogeneity in the Sn-based perovskite films, indicated by the elevated full width at half maximum of the PL spectra in Fig. 3c, this element can be associated with localized and/or free excitons, whose decay time is expressed as $1/\tau_1 = 1/\tau_{Xr} + 1/\tau_{nr}$, where τ_{Xr} represents the excitation radiative lifetime and snr denotes the non-radiative trap-assisted recombination time. The detected rise in τ_1 validates the decrease of nonradiative recombination centers. Conversely, τ_2 may be provisionally linked to bimolecular (band-to-band) recombination through radiation and is similarly constrained by identical non-radiative pathways, resulting in the observed elongation. $MXG/FAMASnI_3$ (3.6 ns) > $MX/FAMASnI_3$ (2.8 ns) > $FASnI_3$ (1.1 ns) (refer to Table S1) highlights the enhanced quality of the films upon the incorporation of additives [50].

To investigate the impact of MXG on the photovoltaic performance of perovskite solar cells, it is crucial to clarify the microscopic structure of

the perovskite films. The AFM study reveals a clear tendency of the surface roughness reduction when the film composition changes from pure $FAMASnI_3$ film to MXene modified and to MXG inclusion. $FAMASnI_3$ (Fig. 4a) shows large coarsely packed grains with well-defined surface valleys and peaks indicating significant topographical protrusions and higher roughness (RMS = 36.5 nm) that can block the interfacial contact for trap-assisted recombination. Conversely, MX/$FAMASnI_3$ (Fig. 4 b) shows improved grain regularity and reduced height disparity, indicating the role of MXene flakes in alleviating the surface roughness (RMS = 30.1 nm) by working out as heterogeneous nucleation sites. Significantly, MXG/$FAMASnI_3$ (Fig. 4 c) possesses the most uniform and densely packed grain formation with the smallest change in surface height profile, implying the least roughness, i.e. RMS for this sample is 26.6 nm compared to the other two samples. This

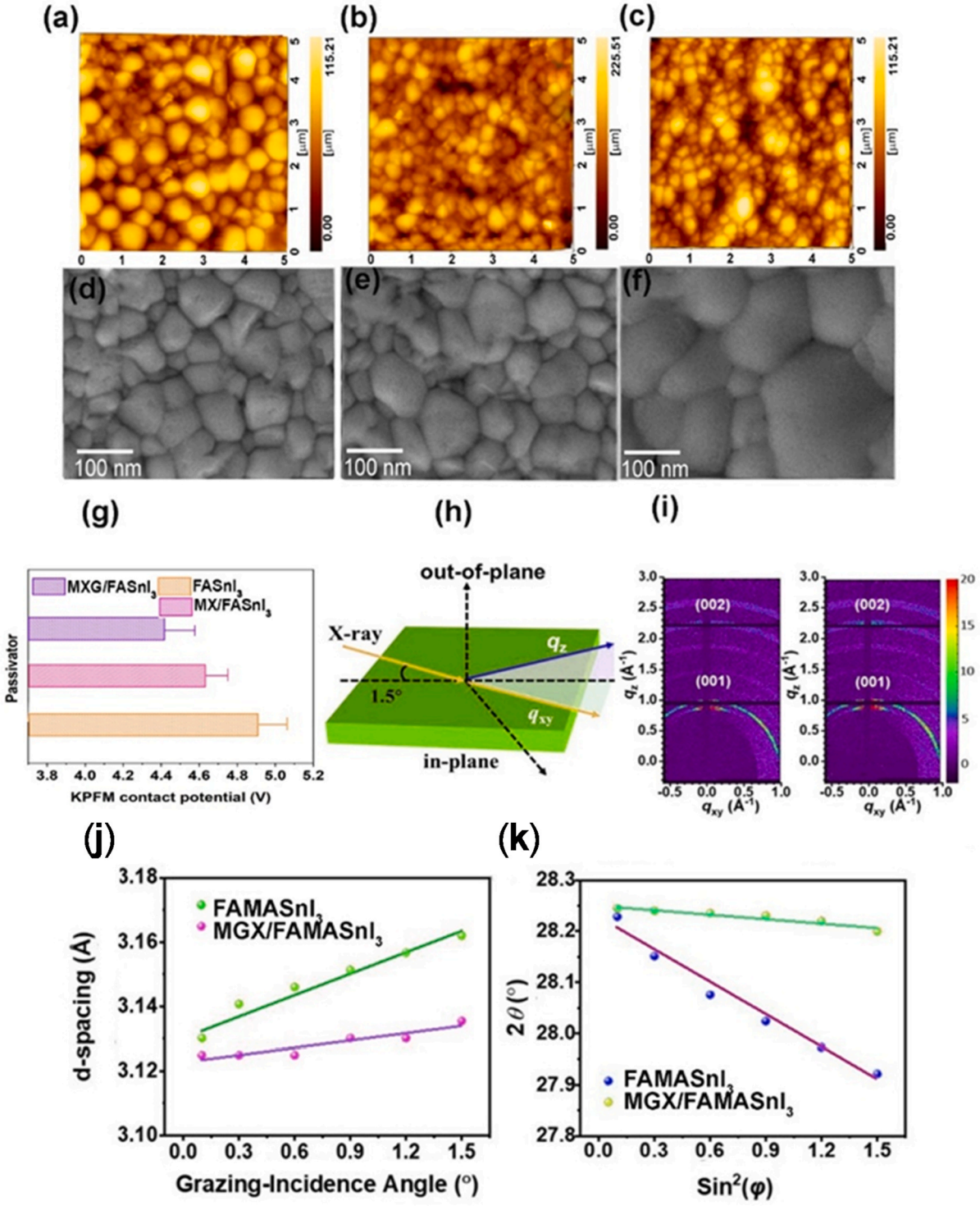

Fig. 4. Morphological, structural, and surface electronic property analysis of $FAMASnI_3$, MX/$FAMASnI_3$, and MXG/$FAMASnI_3$ perovskite films. (a–c) AFM images, (d–f) SEM images, (g) KPFM-derived surface contact potential values $FAMASnI_3$, MX/$FAMASnI_3$, and MXG/$FAMASnI_3$ perovskite films, (h) Schematic of grazing-incidence wide-angle X-ray scattering (GIWAXS), (i) 2D GIWAXS patterns of $FAMASnI_3$ and MXG/$FAMASnI_3$, (k) d-spacing variation versus grazing-incidence; (l) of strain analysis (2θ vs $\sin^2\varphi$) MXG/$FAMASnI_3$.

observation can be attributed to the ability of glycine as a nucleic control agent and improved films wetting behavior for creation of uniform texture with smaller size, smooth morphology that allow effective charge transport and interface stability. SEM images (Fig. 4d–f) also confirm that adding MXG leads to denser and larger grains with fewer voids, which favours the film quality and mechanical strength. For the efficiency of perovskite solar cells, efficient extraction of carrier and minimal energy loss at the interface were crucial. As a result, it is crucial to tune the surface potential of perovskite layer for better matching with adjacent transport layers. A higher surface potential (or lower the Fermi level) at perovskite side might induce more preferable band alignment towards the ETL to facilitate electron extraction and suppress recombination losses. Kelvin Probe Force Microscopy (KPFM) is a non-destructive, surface-specific technique that measures the contact potential difference (CPD) between a conductive AFM tip and the sample. This work function-related CPD is critical for the knowledge of positions on the Fermi level, surface dipoles and band alignment that are necessary for materials useable as charge transport/extraction layers in solar systems. The KPFM study provides (Fig. 4g) important information about the interfacial electronic behavior of $FASnI_3$, MX/$FASnI_3$, and MXG/$FASnI_3$ films: C on the top surface due to contact potential measurement. Device characterization of pristine $FASnI_3$ reveals a low contact potential of 4.35 eV, suggesting a shallow work function with potential surface Fermi level pinning likely due to a high defect density such as Sn^{4+} and iodine vacancies. The inclusion of MXene (4.45 V) leads to small enhancement of the surface potential, which is attributed to partial passivation of bandgap states at the surface and dipole fields from the surface terminations between MXene and phosphorene. The most significant change is observed for the MXG/$FASnI_3$ film, which has the largest surface potential (~4.85 V), indicative of a substantially higher Fermi level. This enhancement is because of the double role of glycine zwitterionic-type functional groups that are effective in passivating defects and favorable interfacial dipoles for tuning vacuum level. The result is improved energy level alignment with electron transport layers, facilitating more efficient charge extraction, reducing the interfacial recombination and increasing built-in electric field [51].

The grazing-incidence X-ray diffraction (GIXRD)-based analysis also confirms the advantageous effect of MXG functionalization on structural changes occurring in the $FAMASnI_3$ perovskite film. Compared with the pure $FAMASnI_3$, the MXG/$FAMASnI_3$ films have better crystallinity and more remarkable out-of-plane orientation (Fig. 4i). Features of the (001) and (002) diffraction are enhanced. Such alignment is required since the stronger (001)/(002) reflections demonstrate that the granules are neatly stacked along the vertical direction, allowing carriers to migrate throughout the device structure. The d-spacing analysis (Fig. 4k) indicates that the pristine $FAMASnI_3$ film had a strong ion δ glide from around 3.12 Å to ~3.16 Å, while increasing the grazing incidence angle. This change indicated that there exists a nonuniform lattice expansion and residual tensile strain. In contrast, the MXG/$FAMASnI_3$ film showed a slight difference in changed d-spacing (from 3.12 Å to 3.13 Å) and flatter slope shape of d-spacing fitting line means a more uniform crystal lattice and lower vertical strain gradient. This indicates that the MXG modification suppresses the anisotropic tension in film forming by controlling a uniform vertical grain growth.

The addition of MXG did not alter the solubility of SnI_2 or FAI in the DMF/DMSO precursor, as demonstrated by the consistent precursor absorption profile and the same optical band edge in all samples (Fig. 3c). Nonetheless, MXG exerts a substantial impact on the crystallization route. In the temperature-assisted XRD development (Fig. 3a), MXG/$FASnI_3$ films demonstrate an earlier onset and enhanced intensity of the (100), (120), and (200) reflections, accompanied by a decreased FWHM, signifying expedited nucleation and improved crystal coherence. This activity aligns with heterogeneous nucleation prompted by the surface $–NH_2$ groups of glycine-functionalized MXene, where the Lewis basic sites can temporarily coordinate Sn^{2+} and promote organized precursor–MXG interactions. Additionally, GIWAXS analysis (Fig. 4i) reveals a significant amplification of the (001)/(002) diffraction features and a diminished d-spacing gradient (Fig. 4k), indicating a more distinct vertical orientation and reduced strain in MXG-treated films. This orientation is generally linked to lamellar templating in layered 2D additives, aided by the increased interlayer spacing and high aspect-ratio morphology of MXG (Fig. 2c–e). Collectively, our findings suggest that MXG does not affect precursor solubility but regulates crystallization kinetics via surface dipoles, Lewis-basic interactions, and lamellar templating, resulting in vertically aligned grains with less strain and enhanced structural uniformity.

High-resolution TEM (HRTEM) was used to explore the microstructural features of the MXG–$FAMASnI_3$ heterojunction (Fig. 5a and b), and HAADF elemental mapping (Fig. 5c) was performed to visualize how MXG is distributed within the perovskite film. The TEM images clearly show that the glycine-functionalized MXene (MXG) integrates closely with the $FAMASnI_3$ grains. In Fig. 5a, the layered, slightly crumpled morphology of MXG appears to support and interlace with the surrounding perovskite crystals, suggesting that MXG acts as a conductive scaffold that promotes uniform crystal growth. The high-resolution image in Fig. 5b further confirms the tight physical contact between MXG and the perovskite, a feature that is crucial for efficient charge transfer and maintaining a stable interface. Elemental mapping (Fig. 5c) shows a well-mixed distribution of key elements-F and Ti from MXG, Sn and I from the perovskite, and O and N likely contributed by both glycine and the $FAMASnI_3$ lattice. The absence of visible phase separation indicates effective chemical interaction and hybrid formation. Altogether, these observations suggest that MXG not only reinforces the composite structure but also contributes chemical functionality that helps passivate defects and improve electronic coupling. This morphology-driven interfacial synergy ultimately supports better carrier transport, reduces recombination losses, and enhances the overall stability of perovskite optoelectronic devices.

The space-charge limited current (SCLC) technique was used to quantify the defect state density N_t as shown in Fig. 6a. The value of N_t was obtained from Equation (2)

$$N_t = \frac{2\varepsilon\varepsilon_0 V_{TFL}}{qL^2} \tag{2}$$

Here, L denotes the thickness of the perovskite film, ε_0 is the vacuum permittivity, ε represents the relative dielectric constant of the perovskite, and V_{TFL} refers to the trap-filling voltage. The V_{TFL} values for the pristine and target devices are 0.71 V and 0.50 V, with N_t values of 3.61 $\times 10^{15}$ cm^3 and 2.72 $\times 10^{15}$ cm^3, respectively [52]. A lower bias voltage required to attain the second segment of the trap filling limit area corresponds to a reduced number of carriers inserted into the defect state [53–55]. The reduction in N_t can be adequately elucidated by the target film's preferential growth orientation, the enlargement of grain size, and the diminished defect density, which collectively account for the elevated fill factor (FF).

EIS was applied to the study of the interfacial charge dynamics of $FAMASnI_3$ and MXG/$FAMASnI_3$ devices. The Nyquist plots (Fig. 6d) have provided an in-depth analysis of their charge transport and recombination properties. Both plots feature a classical semicircle in the mid-frequency range, and a low-frequency tail related to ion migration and recombination. The semicircular arc of MXG/$FAMASnI_3$ is much smaller than that of pristine $FAMASnI_3$, indicating a great decrease in R_{ct} from ~2.97 $\times$ 10^3 Ω with $FAMASnI_3$ to 1.21 $\times$ 10^3 Ω with MXG/$FAMASnI_3$. This indicates the higher efficiency of interfacial charge extraction and recombination suppression [56]. This enhancement is attributed to improved energy level alignment and trap passivation at the perovskite/MXG interface. Moreover, the double-layer capacitance (C_{dl}) increased (from ~4.1 μF to ~5.2 μF), and the series resistance (R_s) marginally decreased (from ~12.6 Ω to ~11.2 Ω). These changes are indicative of improved interfacial dielectric properties and increased charge accumulation at the interface. These results are consistent with

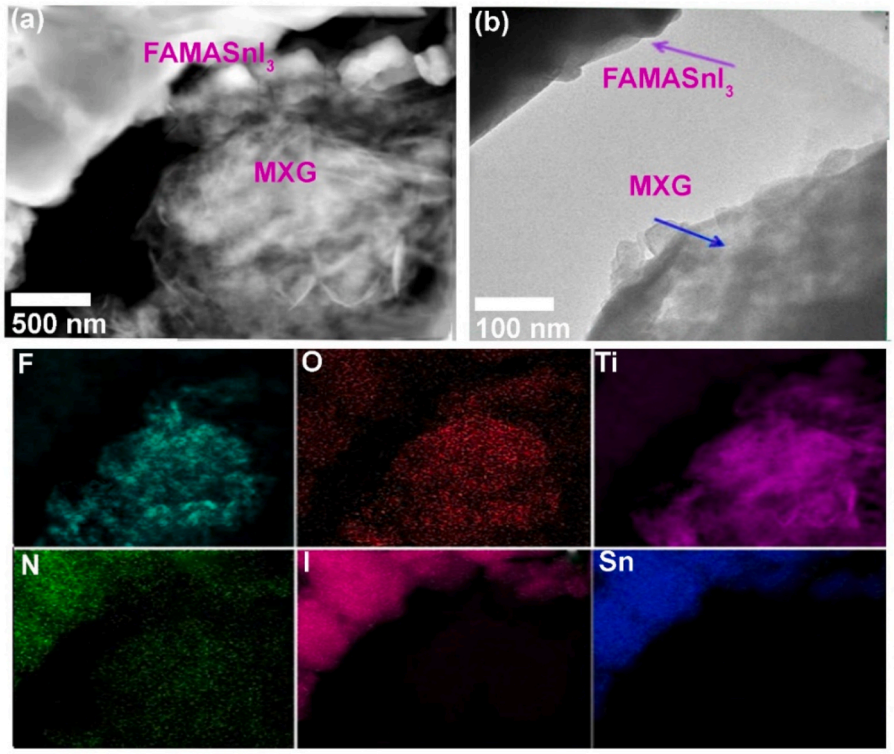

Fig. 5. Morphological and elemental distribution analysis of the MXG/FAMASnI$_3$, hybrid composite. (a) TEM, (b) HRTEM images of MXG/FAMASnI$_3$, (c) Elemental mapping via energy-dispersive X-ray spectroscopy of MXG/FAMASnI$_3$.

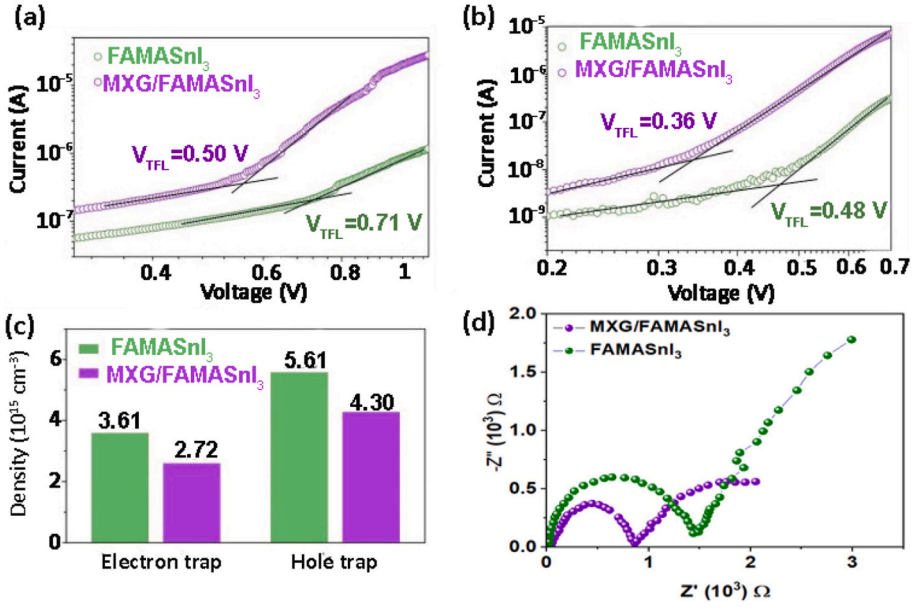

Fig. 6. (a, b) Space-charge-limited current (SCLC) measurements of hole-only (a) and electron-only (b) devices for FAMASnI$_3$ and MXG/FAMASnI; (c) comparison of calculated trap densities (N_t) for both electron and hole traps, revealing reduced trap density in MXG-modified devices. (d) Nyquist plots from EIS.

the SCLC analysis, which demonstrated that the trap densities in MXG-modified films were reduced. These results collectively validate the notion that the introduction of glycine-functionalized MXene results in improved optoelectronic quality, reduced recombination losses, and more efficient carrier transport in the perovskite device architecture [57]. The extended photoluminescence decay lifespan noted in MXG/FASnI$_3$ (Fig. 3d) indicates a decrease in bulk trap-assisted recombination and improved carrier extraction at the perovskite/transport-layer interface. The rapid component τ_1 escalates from 0.4 ns (FASnI$_3$) to 1.45 ns (MX/FASnI$_3$) and 2.12 ns (MXG/FASnI$_3$), signifying the attenuation of interfacial nonradiative routes typically linked to under-coordinated Sn and iodide vacancies. The slow component τ_2, associated with band-to-band recombination, shows a comparable rise, in accordance with the reduced defect density measured by SCLC (Fig. 6c). Furthermore, KPFM analysis (Fig. 4g) indicates that MXG displaces the Fermi level to lower values, enhancing

energetic alignment with the PCBM electron-transport layer, whereas EIS spectra (Fig. 6d) demonstrate a significantly reduced charge-transfer resistance in MXG-modified devices. The results indicate that MXG decreases trap density in the perovskite bulk and improves interfacial charge transfer by establishing a more advantageous band offset and inhibiting recombination at the perovskite/PCBM interface. The simultaneous enhancement in interfacial energetics and defect passivation accounts for the markedly extended TRPL lifetimes and directly influences the elevated Voc and FF of MXG-treated devices.

The comprehensive optoelectronic and energy-level characterization presented in Fig. 7 provides critical insights into the effects of MXG incorporation on the structural and electronic quality of $FAMASnI_3$ films. The lower energetic disorder and a diminished density of sub-bandgap states in MXG/$FAMASnI_3$ (34.43 meV) compared to pristine $FAMASnI_3$ (45.75 meV) (Fig. 7a) are consistent with suppressed trap-assisted non-radiative recombination; this is evidenced by the reduced Urbach energy (E_u). The Mott–Schottky diagrams (Fig. 7b) indicate that MXG/$FAMASnI_3$ has a higher built-in potential ($V_{bi} = 0.82$ V) and built-in electric field. This promotes efficient carrier separation and reduces recombination losses, thereby contributing to an enhanced V_{oc}. Furthermore, the Tauc plots (Fig. 7c) demonstrate a marginal bandgap reduction as a result of the addition of MXG. The UPS analysis (Fig. 7b) further verifies the favorable energy-level alignment in MXG/$FAMASnI_3$. This alignment implies a somewhat deeper valence band maximum (−5.51 eV) and a lower work function (16.76 eV), which facilitate hole extraction and decrease interfacial energy barriers. The quality of the 3D domains with larger diffusion lengths was very good due to the controlled templating during crystallization. As a result, the energy-level diagrams (Fig. 7c) show how the MXG alteration improves the conduction and valence bands of $FAMASnI_3$. This makes it easier for transport layers (such PEDOT and PCBM) to line up and lets carriers move in a balanced way. In general, these synergistic effects like fewer trap states, better band alignment, higher built-in potential, and lower Urbach energy show how important MXG is for changing the electrical microenvironment of $FAMASnI_3$.

Inspired by the enhanced crystalline and film morphology, we developed tin-based perovskite solar cells using an inverted (p–i–n) architecture of ITO/PEDOT:PSS/$FASnI_3$/PCBM/Ag (see Methods for detailed materials). As shown in Fig. 8a, b the optimal perovskite absorber layer had a thickness of about 300 nm. The champion MXG/$FASnI_3$ device attained a power conversion efficiency (PCE) of 15.82 % by evaluating the current density–voltage (J–V) characteristics under standard AM 1.5G simulated sunlight, exhibiting an open-circuit voltage (V_{oc}) of 0.98 V, a short-circuit current density (J_{sc}) of 23.47 mA cm^{-2}, and a fill factor (FF) of 75.7 % (Fig. 8c). The control $FASnI_3$ device had a reduced PCE of 12.63 %. The MXG/$FASnI_3$ device achieved a steady power conversion efficiency of 15.61 % under maximum power point tracking, surpassing the 12.41 % of the reference device. The external quantum efficiency (EQE) spectra (Fig. 8d) demonstrated an augmented photocurrent response in the MXG/$FASnI_3$ device throughout the visible spectrum, yielding an integrated Jsc of 22.81 mA cm^{-2}, which closely aligns with the J–V measurements. The MXG-based devices in a batch of uniformly fabricated devices showed an enhanced average PCE 15.8 ± 0.29 %, which highlights the beneficial role played by MXG in improving not only device efficiency but also consistency. In addition, little hysteresis was observed (Fig. 8e), and a hysteresis of 3.1 %, which may be attributed to suppressed ion migration by improved surface passivation from the glycine-functionalized MXene layer. Long-term stability testing in (Fig. 8f) we find that the incorporation of MXG maintains more than 94 % initial PCE over 1000 h, which exceeds pristine $FASnI_3$. Fig. 8g and h also verifies the boosted PCE and higher J_sc are consistent, which strongly proves that trap states can be efficiently passivated by MXG while enhancing interfacial charge dynamics. Together, these results demonstrate the potential of MXG as an interfacial engineering strategy for improving Sn-based perovskite PV performance and reliability.

As for the durability at a high temperature, Fig. S1 summarizes the photovoltaic performance and high temperature operation stability of the optimized MXG/$FASnI_3$ device. The J–V characteristics (Fig. S1a), which show a large short-circuit current density (J sc ≈ 23–24 mA cm^{-2}), open-circuit voltage (V oc ≈ 0.95–1.0 V) and fill factor over 70 %, reaching power conversion efficiency (PCE) of about 15–16 %. The forward and reverse scans exhibit small hysteresis, indicating that the MXG interfacial layer effectively suppresses the ion migration,

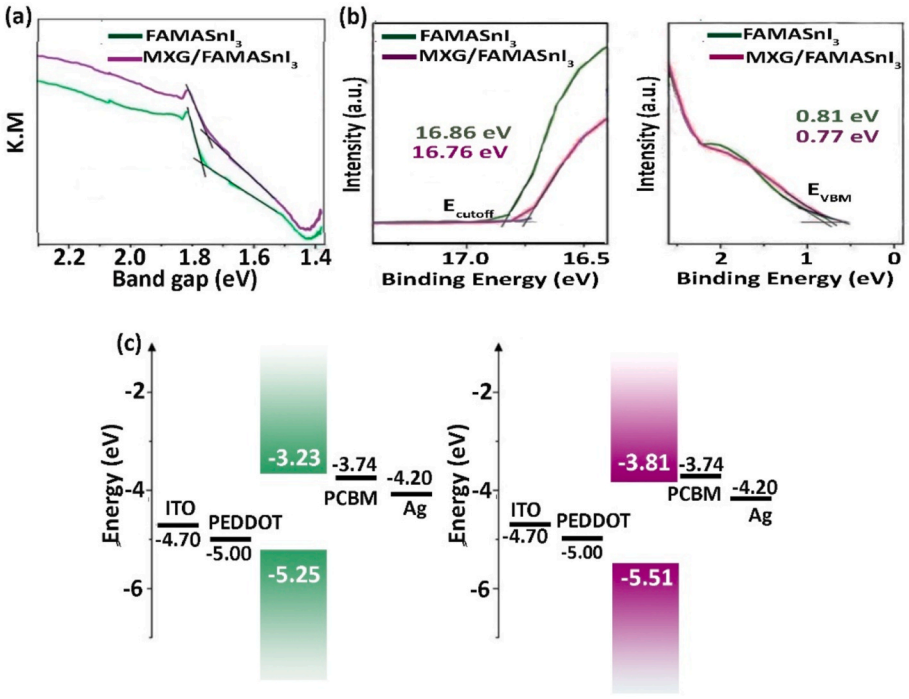

Fig. 7. (a) Tauc plots and (b) UPS spectra for $FASnI_3$ and MXG/$FASnI_3$ films. (c) Energy level alignment diagrams of the inverted (p–i–n) device structure for $FASnI_3$ (left, green) and MXG/$FASnI_3$ (right, purple).

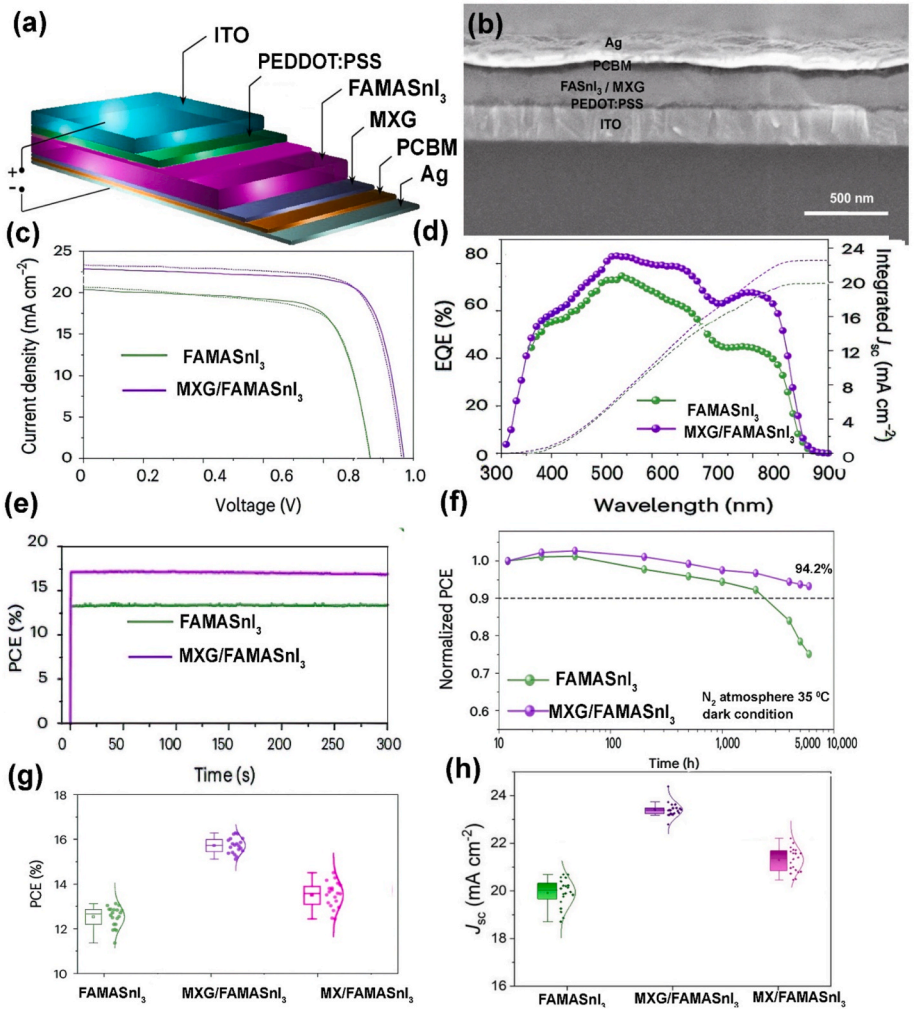

Fig. 8. (a) Schematic illustration of the device architecture for inverted (p–i–n) perovskite solar cells incorporating the MXG interface layer. (b) Cross-sectional SEM image of the MXG/FAMASnI$_3$. (c) J–V curves (d) External quantum efficiency (EQE). (e) Stabilized power output showing higher steady-state performance for MXG/FASnI$_3$. (f) Normalized PCE) over time under N_2 atmosphere and dark storage at 35 °C, demonstrating enhanced operational stability in MXG/FASnI$_3$ devices. (g) Statistical PCE distribution of over 15 devices showing improved reproducibility. (h) Box plot of short-circuit current density (J_sc) confirming enhancement with MXG incorporation.

capacitive charging effects of which are generally improved in Sn-based perovskite devices at high temperatures. The EQE spectrum (Fig. S1b) demonstrates a strong photo-response from 350 to 900 nm, with a smooth and monotonous photocurrent integration curve that overlaps with the J–V-derived Jsc. The lateral EQE rise from 450 to 650 nm shows an improved carrier extraction in the visible region, as initiated by MXG-mediated trap reduction and interfacial band tuning. The integrated J sc fits well with the J–V characterization, thus corroborating the accuracy of the device data. During unceasing operation (Fig. S1c), the stable power conversion efficiency and output current can be retained for 1000 s at max-power-point-equivalent biasing. The low drift (<3 %) implies suppressed ionic redistribution and excellent thermal–electrical coupling, both usually worse in Sn-based perovskites because of the ease of thermal oxidation of Sn^{2+}. The MXG layer contributes to the thermal stabilization of Sn 4+ by reducing labile defect sites, which promote the oxidation of Sn $2+^{+}$ to Sn^{4+}, even under severe stress. The long term thermal stability at 130 °C (Fig. S1d) shows one of the key advantages of MXG incorporation. The bottom curve in Fig. 4 shows the normalized PCE that is still maintained at more than 80–85 % of its original value after aging for 1200 h at the elevated temperature and with values exceeding the temperature normally used during standard perovskite certification tests (typically, 85 °C). This resistance indicates that MXG not only passivates under-coordinated Sn and iodine-vacancy defects as well as impedes subgrating boundaries, contributing to the solar cell s record temperature stability, but it also improves both the structural and electrical integrity of the perovskite lattice during extreme T (−70 °C) stress. The weak performance decay could be attributed to the slowly growing bulk defects over time stages or partial decay of the volatile surface species, but it is far more stable than traditional FASnI$_3$ devices (~ a few weeks), which usually degrade quickly by tin oxidation in an accelerated manner and structural collapse.

5. Conclusion

The research proposes a dual-functional strategy that applies the glycine-attached $Ti_3C_2T_x$ MXene (MXG) in order to tackle the limitations of lead-free FASnI$_3$ perovskite solar cells. The amino-functionalized MXene is simultaneously working to release trapped charge carriers and to stop Sn oxidation by getting into a chemical interaction with the Sn atoms that are not fully coordinated and acting as a mild reductant. The MXene-based scaffold acts as a conductive 2D structure that supports the process of perovskite crystallization being uniform, giving the coming up of grains in the vertical direction, lowering the loss of light due to rough surface, and providing good contact for electronic transport at the interface. These combined actions lead to huge enhancements

in the areas of film morphology, carrier dynamics, and energy-level alignment. The devices that use MXG were able to reach the highest power conversion efficiency of 15.82 %, exhibited very little hysteresis, and showed a long-term stability of 94 % retention after 1000 h. The results point to the remarkable multifunctional properties of MXenes, which can act as chemical passivators and at the same time, structural and electrical modulators, thus offering a friendly to the environment, easily scalable solution for the coming generation of lead-free perovskite solar cells.

CRediT authorship contribution statement

Aseel j. Mohammed: Writing – original draft, Supervision, Software, Project administration, Methodology, Data curation, Conceptualization. **Wala Dizayee:** Writing – original draft, Software, Project administration, Methodology, Investigation, Funding acquisition, Formal analysis, Data curation, Conceptualization. **Ismail Ibrahim Marhoon:** Validation, Supervision, Software, Resources, Methodology, Investigation, Formal analysis, Data curation, Conceptualization. **Mohammed Ahmed Mohammed:** Writing – original draft, Software, Resources, Project administration, Methodology, Investigation, Funding acquisition, Formal analysis, Data curation, Conceptualization. **Mohammed Zorah:** Validation, Supervision, Software, Project administration, Investigation, Funding acquisition, Formal analysis, Data curation, Conceptualization. **Zainab Shaker Matar Al-Husseini:** Writing – review & editing, Visualization, Validation, Supervision, Software, Resources, Project administration, Methodology, Investigation, Conceptualization. **Mohamed Shabbir Abdulnabi:** Visualization, Supervision, Software, Resources, Project administration, Methodology, Funding acquisition, Data curation, Conceptualization. **G. Abdulkareem-Alsultan:** Writing – review & editing, Writing – original draft, Supervision, Software, Methodology, Investigation, Data curation, Conceptualization. **Maadh Fawzi Nassar:** Writing – review & editing, Writing – original draft, Visualization, Validation, Supervision, Software, Resources, Project administration, Methodology, Investigation, Funding acquisition, Formal analysis, Data curation, Conceptualization.

Declaration of competing interest

The authors declare that they have no known competing financial interests or personal relationships that could have appeared to influence the work reported in this paper.

Acknowledgments

We would like to thank all authors.

Appendix A. Supplementary data

Supplementary data to this article can be found online at https://doi.org/10.1016/j.jsamd.2025.101085.

References

[1] F. Alshaeer, M.A. Mohammed, M. Zorah, N. Alharbi, H.M.A. Mahmoud, A.M. E. Ahmed, B.A. Mohammed, G. Abdulkareem-Alsultan, M.F. Nassar, Synergistic defect passivation and charge transport enhancement via thiosemicarbazide-functionalized carbon nanotubes for high-efficiency lead-free $CsSnI_3$ perovskite solar cells: a pathway to 23.34 % efficiency, J. Alloys Compd. 1026 (2025) 180428, https://doi.org/10.1016/j.jallcom.2025.180428.

[2] W. Yu, Y. Zou, H. Wang, S. Qi, C. Wu, X. Guo, Y. Liu, Z. Chen, B. Qu, L. Xiao, Breaking the bottleneck of lead-free perovskite solar cells through dimensionality modulation, Chem. Soc. Rev. 53 (2024) 1769–1788, https://doi.org/10.1039/D3CS00728F.

[3] Y. Liu, T. Ma, C. Wang, Z. Yang, Y. Zhao, Z. Wu, C. Chen, Y. Bao, Y. Zhai, T. Jia, C. Chen, D. Zhao, X. Li, Synergistic immobilization of ions in mixed tin-lead and all-perovskite tandem solar cells, Nat. Commun. 16 (2025) 3477, https://doi.org/10.1038/s41467-025-58810-6.

[4] R.A. Lashaki, Z. Raeisi, M. Makki, S. Zare, Dendrite neural network scheme for estimating output power and efficiency for a class of solar free-piston Stirling engine, Int. J. Model. Simulat. (2025) 1–12, https://doi.org/10.1080/02286203.2025.2459989.

[5] C. Qiu, J. Song, Y. Wu, X. Yin, L. Hu, Z. Su, Y. Jin, W. Wang, H. Wang, Z. Li, Defect passivation via a multifunctional organic additive toward efficient and stable inverted perovskite solar cells, Chem. Commun. 59 (2023) 6414–6417, https://doi.org/10.1039/D3CC01002C.

[6] M. Xia, Z. Zheng, Y. Cheng, C. Wang, Z. Cui, G. Zhang, J. Gong, A. Mei, H. Han, Tailored multifunctional hydrazine derivatives for efficient printable hole-conductive-free mesoscopic perovskite solar cells via enhancing defect passivation, J. Energy Chem. 95 (2024) 357–363, https://doi.org/10.1016/j.jechem.2024.03.051.

[7] F. Alshaeer, M.A. Mohammed, M. Mohammed, N. Alharbi, H.M.A. Mahmoud, A.M. E. Ahmed, B.A. Mohammed, G. Alsultan, M.F. Nassar, Synergistic defect passivation and charge transport enhancement via thiosemicarbazide-functionalized carbon nanotubes for high-efficiency lead-free $CsSnI_3$ perovskite solar cells: a pathway to 23.34 % efficiency, J. Alloys Compd. (2025) 1026, https://doi.org/10.1016/j.jallcom.2025.180428.

[8] Z. Huang, A.H. Proppe, H. Tan, M.I. Saidaminov, F. Tan, A. Mei, C.-S. Tan, M. Wei, Y. Hou, H. Han, S.O. Kelley, E.H. Sargent, Suppressed ion migration in reduced-dimensional perovskites improves operating stability, ACS Energy Lett. 4 (2019) 1521–1527, https://doi.org/10.1021/acsenergylett.9b00892.

[9] W. Zeng, E. Li, J. Li, L. An, Y. Shi, Q. Niu, K. Ocakoglu, T. Yang, X. Peng, R. Xia, Self-repairing tin-based perovskite solar cells using 2,4-dichlorophenylhydrazine hydrochloride as dopant, Synth. Met. 312 (2025) 117882, https://doi.org/10.1016/j.synthmet.2025.117882.

[10] Z. Zhang, Z. Su, G. Li, J. Li, M.H. Aldamasy, J. Wu, C. Wang, Z. Li, X. Gao, M. Li, A. Abate, Improved air stability of tin halide perovskite solar cells by an N-Type active moisture barrier, Adv. Funct. Mater. 34 (2024) 2306458, https://doi.org/10.1002/adfm.202306458.

[11] X. Mu, Y. Liu, G.B. Xiao, C. Xu, X. Gao, J. Cao, Porphyrin supramolecule as surface carrier modulator imparts hole transporter with enhanced mobility for perovskite photovoltaics, Angew. Chem. 62 (2023) e202307152, https://doi.org/10.1002/anie.202307152.

[12] Y. Sun, Y. Li, W. Chen, Z. Sun, Hydrazine acetate promoted the formation of equiaxed perovskite grains for efficient solar cells, J. Mater. Chem. C 13 (2025) 12986–12993, https://doi.org/10.1039/D5TC00561B.

[13] Y. Xing, J. Xiong, Q. Wang, C. Wang, L. Huang, X. Liu, Q. Tai, Y. Zhu, J. Zhang, Selection of phenyl hydrazine derivatives as an Sn4+ reductant for tin–lead perovskite solar cells, J. Mater. Chem. C 12 (2024) 10585–10591, https://doi.org/10.1039/D4TC00719K.

[14] S. Thakur, D.S. Mann, S.S. Sangale, S.-N. Kwon, S.-I. Na, Hydrazine derivative-based surface passivator for efficient and stable perovskite solar cells, J. Power Sources 630 (2025) 236124, https://doi.org/10.1016/j.jpowsour.2024.236124.

[15] B. Nabavi, S. Jafari Ghalekohneh, K.J. Shayegan, E.J. Tervo, H. Atwater, B. Zhao, High-temperature strong nonreciprocal thermal radiation from semiconductors, ACS Photonics 12 (2025) 2767–2774, https://doi.org/10.1021/acsphotonics.5c00365.

[16] F. Alshaeer, L.K. Obeas, M. Mohammed, H.M.A. Mahmoud, L.M. Abdalgadir, A. G. Taki, B.A. Mohammed, G. Alsultan, M.F. Nassar, Bandgap-engineered MXene-g-C3N4 interfacial layer for enhanced charge carrier dynamics in perovskite solar cells, J. Alloys Compd. (2025) 1011, https://doi.org/10.1016/j.jallcom.2024.178247.

[17] N. Alharbi, M.M. Alotaibi, L.K. Obeas, I.I. Marhoon, M. Zorah, A.G. Taki, B. A. Mohammed, G. Abdulkareem-Alsultan, M.F. Nassar, Boosting efficiency and long-lifespan in perovskite solar cells via 2D-MXene/Janus MoSSe integration, J. Alloys Compd. 1013 (2025) 178501, https://doi.org/10.1016/j.jallcom.2025.178501.

[18] S. Marimuthu, A.P. Shyma, S. Sathyanarayanan, T. Gopal, J.T. James, S. P. Nagalingam, B. Gunaseelan, S. Babu, R. Sellappan, A.N. Grace, The dawn of MXene duo: revolutionizing perovskite solar cells with MXenes through computational and experimental methods, Nanoscale (2024), https://doi.org/10.1039/D4NR01053A.

[19] W. Dizayee, M.M. Hamarashid, M. Mohammed, H.M.A. Mahmoud, M. Al-Bahrani, A.G. Taki, G. Alsultan, M.F. Nassar, Synergistic effect of Ni(OH)2 and MXene nanosheets in 3D framework on the improvement of dielectric, energy storage, mechanical and thermal characteristics of polyvinylidene fluoride(PVDF) polymeric composites, J. Alloys Compd. (2024) 1004, https://doi.org/10.1016/j.jallcom.2024.175825.

[20] K.A. Abaid Samawi, B.A. Mohammed, E.A.A. Abd-Alkuder Salman, H.M. A. Mahmoud, A.Z. Zuhair Sameen, S.M. Mohammad Mohealdeen, G. Alsultan, M. F. Nassar, Vertical growth of a 3D Ni-Co-LDH/N-doped graphene aerogel: a cost-effective and high-performance sulfur host for Li-S batteries, Phys. Chem. Chem. Phys. 26 (2024) 9284–9294, https://doi.org/10.1039/d3cp05716j.

[21] S. Qamar, K. Fatima, N. Ullah, Z. Akhter, A. Waseem, M. Sultan, Recent progress in use of MXene in perovskite solar cells: for interfacial modification, work-function tuning and additive engineering, Nanoscale 14 (2022) 13018–13039, https://doi.org/10.1039/D2NR02799B.

[22] N. Alharbi, M.M. Alotaibi, L.K. Obeas, I.I. Marhoon, M. Mohammed, A.G. Taki, B. A. Mohammed, G. Alsultan, M.F. Nassar, Boosting efficiency and long-lifespan in perovskite solar cells via 2D-MXene/Janus MoSSe integration, J. Alloys Compd. 1013 (2025), https://doi.org/10.1016/j.jallcom.2025.178501.

[23] F. Alshaeer, M. Zorah, H.M. Mahmoud, L. Abdalgadir, A.G. Taki, B.A. Mohammed, G. Abdulkareem-Alsultan, M.F. Nassar, Bandgap-engineered MXene-g-C3N4 interfacial layer for enhanced charge carrier dynamics in perovskite solar cells,

J. Alloys Compd. 1011 (2024) 178247, https://doi.org/10.1016/j.jallcom.2024.178247.
[24] X. Yao, J. Duan, Y. Zhao, J. Zhang, Q. Guo, Q. Zhang, X. Yang, Y. Duan, P. Yang, Q. Tang, Stretchable alkenamides terminated Ti3C2Tx MXenes to release strain for lattice-stable mixed-halide perovskite solar cells with suppressed halide segregation, Carbon Energy 5 (2023) e387, https://doi.org/10.1002/cey2.387.
[25] M. Javadi, K.M. Jorshary, M. Mazrooie, A. Shojaee, Meta-synthesis method in the field of sustainable industrial production strategies, Journal of Business and Management Studies 7 (2025) 333–343, https://doi.org/10.32996/jbms.2025.7.3.17.
[26] K.A. Abaid Samawi, E.A.A. Abd-Alkuder Salman, H.A. Hasan, H.M.A. Mahmoud, S. M. Mohammad Mohealdeen, G. Alsultan, E. Abdulmalek, M.F. Nassar, Single-atom cobalt encapsulated in carbon nanotubes as an effective catalyst for enhancing sulfur conversion in lithium-sulfur batteries, Molecular Systems Design and Engineering 9 (2024) 464–476, https://doi.org/10.1039/d3me00191a.
[27] M. Faraji, N. Arianpouya, NiCoFe-layered double hydroxides/MXene/N-doped carbon nanotube composite as a high performance bifunctional catalyst for oxygen electrocatalytic reactions in metal-air batteries, J. Electroanal. Chem. 901 (2021) 115797, https://doi.org/10.1016/j.jelechem.2021.115797.
[28] M. Faraji, F. Parsaee, M. Kheirmand, Facile fabrication of N-doped graphene/$Ti_3C_2T_x$ (Mxene) aerogel with excellent electrocatalytic activity toward oxygen reduction reaction in fuel cells and metal-air batteries, J. Solid State Chem. 303 (2021) 122529, https://doi.org/10.1016/j.jssc.2021.122529.
[29] S. Gulnihol, T. Yuldash, R. Kosim, A. Musharraf, L. Abduraximova, I. Zukhra, I. Bakhodir, K. Ra'no, A. Dadaxon, D. Urazbaeva, S. Suluv, M. Faraji, NiFe-LDH-enhanced Ru single-atom catalysts anchored on MXenes for synergistic photothermal–nanocatalytic cancer therapy, Biomater. Sci. 13 (2025) 5685–5704, https://doi.org/10.1039/D5BM01060H.
[30] S. Yousefzadeh, O. Mokhatab, M. Faraji, Enhanced photoelectrocatalytic degradation of tetracycline by g-C_3N_4-TiO_2/Ti_3C_2 Mxene composite modified TiO_2 nanostructures photoelectrode, Inorg. Chem. Commun. 179 (2025), https://doi.org/10.1016/j.inoche.2025.114785.
[31] M. Faraji, S. Yousefzadeh, M.F. Nassar, M.M.A. Zahra, $MnCo_2O_4$/N-doped graphene quantum dot vigorously coupled to MXene nanosheet: a bifunctional oxygen electrocatalyst outperforms Pt/IrO_2 benchmark electrocatalysts in metal-air batteries, J. Alloys Compd. 927 (2022) 167115, https://doi.org/10.1016/j.jallcom.2022.167115.
[32] X. Mao, Y. He, C. Li, H. Li, R. Gou, H. Liu, Y. Zhao, W. Chen, J. Yan, X. Yuan, G. Wu, Glycine–Ti3C2Tx hybrid material improves the electrochemical corrosion resistance of a water-borne epoxy coating, Langmuir 40 (2024) 11817–11827, https://doi.org/10.1021/acs.langmuir.4c01546.
[33] C. Chen, M. Boota, P. Urbankowski, B. Anasori, L. Miao, J. Jiang, Y. Gogotsi, Effect of glycine functionalization of 2D titanium carbide (MXene) on charge storage, J. Mater. Chem. A 6 (2018) 4617–4622, https://doi.org/10.1039/C7TA11347A.
[34] J.H. Heo, F. Zhang, J.K. Park, H. Joon Lee, D.S. Lee, S.J. Heo, J.M. Luther, J. J. Berry, K. Zhu, S.H. Im, Surface engineering with oxidized $Ti_3C_2T_x$ MXene enables efficient and stable p-i-n-structured $CsPbI_3$ perovskite solar cells, Joule 6 (2022) 1672–1688, https://doi.org/10.1016/j.joule.2022.05.013.
[35] M. Ranjbar, S.B. Hezaveh, B. Nabavi, Promoting visible-light degradation of toluene over a simple constructed TiO2/Pd nanocomposite as photocatalytic coating air purification filter, Colloid & Nanoscience Journal 2 (2024) 228–237, https://doi.org/10.61186/CNJ.2.1.228.
[36] Z. NiNi, S.S. Zamir, R. Tojiyev, A. Mamirov, M. Khamrakulova, Y. Karimov, K. Tursunov, L. Kosimov, M. Faraji, Electrospun MXene–Sericin nanofibers for carbonated recycled aggregates: toward intelligent, durable, and low-carbon cementitious composites, Mater. Today Commun. 47 (2025) 113221, https://doi.org/10.1016/j.mtcomm.2025.113221.
[37] E. Abd-Alkuder Salman, K. Abaid Samawi, M. Fawzi Nassar, G. Abdulkareem-Alsultan, E. Abdulmalek, 3D hollow spheres comprising MXene/g-C_3N_4 heterostructre for efficient polysulfide adsorption and conversion in high-performance Li-S batteries, J. Electroanal. Chem. 945 (2023) 117629, https://doi.org/10.1016/j.jelechem.2023.117629.
[38] Z. NiNi, S.S. Zamir, R. Tojiyev, A. Mamirov, M. Khamrakulova, Y. Karimov, K. Tursunov, L. Kosimov, M. Faraji, Electrospun MXene–Sericin nanofibers for carbonated recycled aggregates: toward intelligent, durable, and low-carbon cementitious composites, Mater. Today Commun. 47 (2025), https://doi.org/10.1016/j.mtcomm.2025.113221.
[39] A. Afiqah-Idrus, G. Alsultan, N. Asikin-Mijan, M.F. Nassar, L.H. Voon, S. Teo, T. A. Kurniawan, N. Athirah Adzahar, M. Surahim, S. Razali, A. Islam, R. Yunus, N. Alomari, Y.H. Yap, Deoxygenation of waste sludge palm oil into hydrocarbon rich fuel over carbon-supported bimetallic tungsten-lanthanum catalyst, Energy Convers. Manag. X 23 (2024), https://doi.org/10.1016/j.ecmx.2024.100589.
[40] G. Alsultan, N. Asikin-Mijan, L.K. Obeas, A. Islam, N. Mansir, S. Teo, S. Razali, M. F. Nassar, M. Surahim, Y.H. Yap, Selective deoxygenation of sludge palm oil into diesel range fuel over Mn-Mo supported on activated carbon catalyst, Catalysts 12 (2022), https://doi.org/10.3390/catal12050566.
[41] M. Zakertabrizi, F. Bozorgmehrian, M. Jeong, E. Hosseini, V. Ponce, H. Fallahi, S. Bahadorikhalili, H. Nasrabadi, D. Jarrahbashi, H. Castaneda, A. Asadi, Patterned nanostructures on cathodes: a pathway to stronger, high-energy, high-power Li-Ion batteries, ACS Nano 19 (2025) 38970–38980, https://doi.org/10.1021/acsnano.5c07146.
[42] N. Fayzullaev, M. Keshavarz, M. Omidi, S. Rakhimov, R. Nazirova, S. M. Mohealdeen, H.M.A. Mahmoud, M.F. Nassar, M. Faraji, Enhancing Li-S battery performance by harnessing the power of single atoms on 2D borophene, Electrochim. Acta 521 (2025) 145831, https://doi.org/10.1016/j.electacta.2025.145831.
[43] H. Seyrani, S. Ramezanpour, A. Vaezghaemi, F. Kobarfard, A sequential Ugi–smiles/transition-metal-free endo-dig Conia–ene cyclization: the selective synthesis of saccharin substituted 2,5-dihydropyrroles, New J. Chem. 45 (2021) 15647–15654, https://doi.org/10.1039/D1NJ01159F.
[44] N. Fayzullayev, M. Keshavarz, M. Omidi, S. Rakhimov, R. Nazirova, S. M. Mohammad Mohealdeen, H.M.A. Mahmoud, M.F. Nassar, M. Faraji, Enhancing Li-S battery performance by harnessing the power of single atoms on 2D borophene, Electrochim. Acta 521 (2025), https://doi.org/10.1016/j.electacta.2025.145831.
[45] N. Fayzullaev, M. Keshavarz, M. Omidi, S. Rakhimov, R. Nazirova, S. M. Mohealdeen, H.M. Mahmoud, M.F. Nassar, M. Faraji, Enhancing Li-S battery performance by harnessing the power of single atoms on 2D borophene, Electrochim. Acta 521 (2025) 145831, https://doi.org/10.1016/j.electacta.2025.145831.
[46] H. Yun, Y. Chae, E. Kim, H.K. Kim, S. Jang, M.H. Baik, C.W. Ahn, Y. Lee, Ultra-stable titanium carbide MXene functionalized with heterocyclic aromatic amines, Adv. Funct. Mater. 32 (2022) 2203296, https://doi.org/10.1002/adfm.202203296.
[47] A.N. Kumar, K. Pal, Amine-functionalized stable Nb 2 CT x MXene toward room temperature ultrasensitive NO 2 gas sensor, Mater. Adv. 3 (2022) 5151–5162, https://doi.org/10.1039/D2MA00301E.
[48] D.S. Sulaymonovich, N. Fayzullaev, R. Nazirova, A. Ishankulov, M. Omidi, B.N. Al-Nuaimi, B.O. Khakimboy ugli, K.D. Ikhtiyorovna, M. Mamatqulov, M. Faraji, Single-atom silver-borophene hybrid hydrogels for electrically stimulated wound healing: a multifunctional antibacterial platform, Biomater. Sci. (2025), https://doi.org/10.1039/D5BM00609K.
[49] F. Alshaeer, M. Zorah, H.M. Mahmoud, L. Abdalgadir, A.G. Taki, B.A. Mohammed, G. Abdulkareem-Alsultan, M.F. Nassar, Bandgap-engineered MXene-g-C3N4 interfacial layer for enhanced charge carrier dynamics in perovskite solar cells, J. Alloys Compd. 1011 (2025) 178247.
[50] E.V. Péan, S. Dimitrov, C.S. De Castro, M.L. Davies, Interpreting time-resolved photoluminescence of perovskite materials, Phys. Chem. Chem. Phys. 22 (2020) 28345–28358, https://doi.org/10.1039/D0CP04950F.
[51] A. Hasan, K.A. Abaid Samawi, M.F. Nassar, R. Haddad, A. Roostaie, S. M. Sadeghzadeh, Synthesis of cyclic carbonate from carbon dioxide and epoxides using bicobalt complexes absorbed on DFNS, Catal. Lett. 153 (2023) 2900–2909, https://doi.org/10.1007/s10562-022-04130-z.
[52] Y. Fazeli, Z. Nourbakhsh, S. Yalameha, D. Vashaee, Anisotropic elasticity, spin-orbit coupling, and topological properties of ZrTe(2) and NiTe(2): a comparative study for spintronic and nanoscale applications, Nanomaterials 15 (2025), https://doi.org/10.3390/nano15020148.
[53] G. Nagaraj, M.K. Mohammed, M. Shekargoftar, P. Sasikumar, P. Sakthivel, G. Ravi, M. Dehghanipour, S. Akin, A.E. Shalan, High-performance perovskite solar cells using the graphene quantum dot–modified SnO2/ZnO photoelectrode, Mater. Today Energy 22 (2021) 100853, https://doi.org/10.1016/j.mtener.2021.100853.
[54] F. Sadegh, S. Akin, M. Moghadam, V. Mirkhani, M.A. Ruiz−Preciado, Z. Wang, M. M. Tavakoli, M. Graetzel, A. Hagfeldt, W. Tress, Highly efficient, stable and hysteresis−less planar perovskite solar cell based on chemical bath treated Zn2SnO4 electron transport layer, Nano Energy 75 (2020) 105038, https://doi.org/10.1016/j.nanoen.2020.105038.
[55] R. Yazzaf, S. Ansariashlaghi, M. Asadi, M. Mahdavi, Recent advances in the synthesis of diphenylamine derivatives: from transition-metal-based methods to metal-free approaches, J. Organomet. Chem. 1042 (2025) 123856, https://doi.org/10.1016/j.jorganchem.2025.123856.
[56] M. Sahraei, Y. Askarzadeh, S. Ebrahimzadeh, F. Gorginpaveh, J. McMaine, A. Liaghat, Removal of nitrate and phosphorus in aqueous solutions by MgO-Modified biochars: adsorption isotherms, Remed. J. 36 (2025) e70045, https://doi.org/10.1002/rem.70045.
[57] M. Aali, M. Mansouri, Z. Raeisi, R.A. Lashaki, S. Tavakoli, Introducing a novel temperature measurement to analyze the effect of hybrid cooling methods on improving solar panel performance: an experimental approach, Appl. Therm. Eng. (2025) 125889, https://doi.org/10.1016/j.applthermaleng.2025.125889.